Journal of Materials Chemistry A

RSC Publishing

PAPER

Ab initio thermodynamic study of (Ba,Sr)(Co,Fe)O_3 perovskite solid solutions for fuel cell applications

Cite this: *J. Mater. Chem. A*, 2013, **1**, 14320

David Fuks,*[a] Yuri Mastrikov,[bc] Eugene Kotomin[bd] and Joachim Maier[d]

Received 24th July 2013
Accepted 25th September 2013

DOI: 10.1039/c3ta12874a

www.rsc.org/MaterialsA

(Ba,Sr)(Co,Fe)O_3 (BSCF) perovskite solid solutions are promising materials for solid oxide fuel cell cathodes and oxygen permeation membranes. Cathode performance strongly depends on the morphology of these materials remaining as a single phase or two-phase mixture. Combining *ab initio* calculations of the atomic and electronic structure of different supercells with thermodynamics of solid solutions, we have constructed and discussed phase diagrams of several important BSCF chemical compositions. It is demonstrated that in BSC cobaltite solid solution the spinodal decomposition may occur already at relatively low temperatures, while ferrite (BSF and SCF) solid solutions decompose at relatively high temperatures forming a two-phase system where the coexisting hexagonal and cubic phases significantly differ in fractions of constituents.

Introduction

Currently ABO_3-type cubic perovskite solid solutions, *e.g.* $Ba_xSr_{1-x}Co_{1-y}Fe_yO_{3-\delta}$ (BSCF), are considered to be promising materials for applications as cathodes of solid oxide fuel cells (SOFCs), oxygen permeation membranes and oxygen evolution catalysis.[1–4] The small oxygen vacancy formation energy characteristic of BSCF leads to high oxygen vacancy concentration,[5,6] whilst a low oxygen vacancy migration barrier causes high ionic mobility.[7] These are two key factors leading to fast oxygen exchange of these materials[1,2,8,9] and hence to their potential role in the context of energy conversion. However, a serious disadvantage of BSCF is its intrinsic instability at intermediate temperatures which leads to a slow transformation into a mixture of several phases, including a hexagonal phase with strongly reduced oxygen diffusivity as well as surface exchange rate.[6,10–13]

Several theoretical studies were performed recently, in order to understand the above-mentioned peculiarities of BSCF,[14–18] the reasons and effects of this structural instability and possible disordering in both A- and B-sublattices of ABO_3-perovskite.[18–20] However, these *ab initio* calculations were performed at 0 K, quite remote from realistic SOFC operational conditions (~1200 K). In this paper, we used *ab initio* calculations as a basis for the thermodynamic study of BSCF solid solutions under realistic external conditions. This approach was successfully applied earlier to similar complex perovskite materials including (Ba,Sr)TiO_3 (BST),[21] (La,Sr)MnO_3 (LSM),[22] (La,Sr)CoO_3 (LSC)[23] and also $Ti_xC_{1-x}N$ alloys.[24] In order to predict the effect of the compositional variation of the multicomponent BSCF, we have constructed three phase diagrams (PDs) for the following solid solutions: $Ba_{1-x}Sr_xCoO_3$ (BSC), $Ba_{1-x}Sr_xFeO_3$ (BSF) ($0 \le x \le 1$) (A-type cations are mixed) and $SrCo_xFe_{1-x}O_3$ (SCF) ($0 \le x \le 1$) (B-type cations are mixed). The changes in the morphology of solid solution with the chemical composition relevant for SOFC operation are analyzed in detail.

In this study, we neglect the oxygen deficiency in the materials, which would introduce much uncertainty into our study focused mainly on the effect of A- and B-site cation composition on solid solution properties. Note that the basic properties of defect-free BSCF and of oxygen vacancies in different concentrations therein were studied in detail in our previous publications[15–18] whereas thermodynamics of oxygen non-stoichiometry in oxygen BSCF is discussed in a separate study.[25]

Method

The results were obtained by means of density functional theory (DFT) as implemented in the computer code VASP 5.2 (ref. 26) with Projector Augmented Wave (PAW) pseudopotentials and the exchange-correlation GGA functional of the PBE-type. We do not use the Hubbard-*U* method here for two reasons. First, our experience[1,14] shows that the DFT in the GGA approximation reliably reproduces the basic structural properties of BSCF and related compounds (see Table 1 below), except for the underestimated band gaps in the insulating states of the parent perovskites. It is also well known that in most cases underestimate of the band gap does not affect the thermodynamic properties of alloys significantly because they are determined by

[a]*Department of Materials Engineering, Ben Gurion University of the Negev, Beer Sheva 84105, Israel. E-mail: fuks@bgu.ac.il*

[b]*Institute of Solid State Physics, University of Latvia, Kengaraga 8, Riga LV-1063, Latvia*

[c]*Materials Science and Engineering Department, University of Maryland, College Park, MD, USA*

[d]*Max Planck Institute for Solid State Research, Heisenbergstr. 1, Stuttgart D-70506, Germany*

Table 1 Calculated cubic and hexagonal lattice parameters $a = b$, c (Å) for three crystalline phases of four parent perovskites, M – magnetic moments of B-cations (μ_B) and the unit cell energy E_c (eV, per 5 atoms). Numbers 2/3 and 1/3 in square brackets show the fraction of non-equivalent B-ions with corresponding spins in the 6H structure. Numbers in () brackets indicate experimental data for lattice parameters and magnetic moments

	Phase	a, b	c	M	E_c
BCO	Cubic	3.97		2.22	−31.79
	2H	5.72(5.65)[f]	4.80(4.76)	0.81	−32.84
	6H	5.67	13.78	1.16[2/3]	−32.26
				2.62[1/3]	
SCO	Cubic	3.84(3.83)[b]		1.75(2.1)	−32.08
	2H	5.46(5.47)[c]	4.74(4.24)	0.82	−32.59
	6H	5.46	13.52	1.24[2/3]	−32.29
				2.58[1/3]	
BFO	Cubic	3.97(3.97)[a]		3.02(3.5)	−34.66
	2H	5.73	4.83	1.74	−35.19
	6H	5.70(5.68)[d]	13.84(13.97)	2.34[2/3]	−34.99
				3.58[1/3]	
SFO	Cubic	3.85(3.85)[e]		2.88(3.1)	−34.97
	2H	5.47	4.78	1.74	−34.90
	6H	5.50	13.59	2.42[2/3]	−35.03
				3.46[1/3]	

[a] Metastable cubic, ref. 40. [b] Metastable cubic, ref. 38. [c] Metastable 2H, ref. 41. [d] Stable 6H phase, ref. 42. [e] Ref. 43. [f] Stable 2H, ref. 30.

integration of the electronic spectra and are less sensitive to the fine structure of the spectra than, let us say, optic, X-ray absorption or magnetic properties.[27] This is more so for formation enthalpies, which are essential for our study, since we calculate mixing energies of solid solutions which are differences of total energies and thus possible GGA inaccuracies are canceled out. Second, use of the Hubbard-U approximation is not applicable for complex perovskite solid-solutions such as BSCF and related materials with very small gaps or metals and containing several types of magnetic ions. Hence, the U parameter fitting would be required for each type of B-sublattice cations. With the lack of experimental data on band gaps of BSC, BSF, SCF, to which the U parameter is usually fitted, there is no existent rigorous procedure for a Hubbard-U optimization. All these make a potential GGA + U approach not only cumbersome, but also unrealistic for these systems.

Note that we do not consider here reduced systems where the application of the GGA approach is more problematic. To demonstrate the quality of our calculations of thermodynamic properties, we calculated the heat of formation of brownmillerite-type $SrFeO_{2.5}$ from two oxides

$$SrO + 1/2Fe_2O_3 = SrFeO_{2.5} \quad (1)$$

The calculated magnitude is 0.54 eV, in good agreement with the experimental estimate of 0.48 ± 0.03 eV (see Table 3 in ref. 28). This justifies the application of the exchange-correlation GGA functional of the PBE-type in our calculations.

The kinetic energy cut-off for the plane wave basis set was set to 520 eV. We start with a study of four parent perovskites – the end members of the BSCF solid solution – $BaFeO_3$ (BFO), $BaCoO_3$ (BCO), $SrFeO_3$ (SFO) and $SrCoO_3$ (SCO). Since these

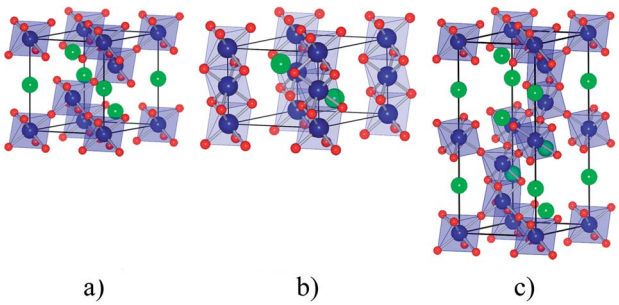

Fig. 1 Schematic view of the ABO_3-type perovskite structures: (a) cubic, (b) 2H- and (c) 6H-hexagonal structures; red, blue and green are oxygen, B-type and A-type atoms, respectively.

materials show different crystal structures—cubic (5 atoms per unit cell) and hexagonal 2H- (10 atoms) or 6H-perovskite phases (30 atoms),[29,30] characterized by face-sharing octahedra and a mixture of face-sharing and corner-sharing octahedra, respectively (Fig. 1), we have calculated all four materials in three phases each and compared with available experimental data.

Solid solutions were modeled using a *supercell model* containing between 40 and 80 atoms. Thus, the total energies for 40-atom cubic structures were calculated using the Monkhorst–Pack scheme[31] with a k-set of 4 × 4 × 4. The hexagonal 2H supercells contained 80 atoms, respectively (k-set 2 × 2 × 3), whereas 6H supercells – 30 atoms (k-set 4 × 4 × 2). For instance, varying the number of Ba atoms from 0 to 8 in the $Ba_xSr_{8-x}Co_8O_{24}$ 40-atom supercell allows us to model a whole range of solid solutions. Due to periodic boundary conditions the alloying elements are periodically arranged through the lattice.

We calculate the Helmholtz free energies of the solid solutions taking into account configurational entropy and neglecting vibrational contributions. In $(Ba_{1-x},Sr_x)CoO_3$ solid solutions Sr atoms substitute for Ba for a whole concentration range, $0 \leq x \leq 1$. This allows us to focus on the alloying sublattice, similar to that in ref. 32 and 33, and to consider the Ba/Sr solid solutions on the sites of a simple cubic (SC) lattice immersed in the external field formed by CoO_3 structural units. Although Sr^{2+} and Ba^{2+} have the same oxidation state, the variation in the atomic fraction of Sr changes the self-consistent charge distribution and thus the electrostatic potential formed by the CoO_3 units. The idea of considering one of the sublattices in the field of the rest of the crystalline lattice was successfully used recently to describe the spinodal decomposition in (Ti,Al)N solid solutions,[32–34] and to predict phase competition in the USi_3–UAl_3 PDs.[35] A similar approach was used to explain the morphology of ultra-thin metal films on a MgO substrate.[36] It was also successfully applied to study the phase equilibrium and to construct the PD for the vacancy-ordered structures of sub-stoichiometric TiC_x alloys.[37]

Main results and discussion

Parent perovskites

The optimized lattice parameters and magnetic moments for the three different phases and B-cation magnetic moments in

four parent perovskites are summarized in Table 1. First of all, the present calculations correctly reproduce the energetically preferable crystalline structures for BCO and SCO (hexagonal 2H). For BFO with a known hexagonal 6H structure we found that the 2H phase is energetically slightly more favorable (by 0.2 eV per ABO_3 formula unit); thus we use this phase in future calculations. The calculated energy for a cubic SFO is very close to that for the 6H structure, and we consider the cubic phase hereafter. Note that in reality the thermodynamic stability of different phases depends strongly also on the material's oxygen stoichiometry; in our calculations we consider fully stoichiometric materials whereas in fact these show some oxygen deficiency. For SCO we compare results for the two phases: cubic and 2H; the former one is metastable but could be prepared by means of electrochemical oxidation of $SrCoO_{2.5}$ at room temperature,[38] whereas the latter one is more stable but also could decompose into two products.[39] In general, agreement between calculations and experiments is quite good, except for the overestimated lattice parameter c for SCO in the 2H phase. (However, the experiments[41] should be independently checked since such a small parameter c contradicts the trend with BCO.) Table 1 shows that the accuracy of our GGA calculations of magnetic moment for the B-type cations in complex perovskites is ~17% for SCO, ~7% for SFO, and ~14% for BFO (metastable cubic phase for which experimental data are available). It means that in the considered compounds the charge transfer from Co/Fe to oxygen is reasonably taken into account. The deviation of calculated magnetic moments from experimental values is small thus giving additional justification to the accuracy of our calculations.

$Ba_{1-x}Sr_xCoO_3$ solid solutions

$Ba_{1-x}Sr_xCoO_3$ (BSC) solid solution was considered as a Ba/Sr sublattice immersed into the field of the rest of the structure consisting of Co and O atoms. To model the $Ba_{1-x}Sr_xCoO_3$ solid solutions with different atomic fractions of Sr on the Ba/Sr sublattice, supercells containing different amounts of Sr were constructed. The lattice parameters of the supercells were optimized through minimization of their total energies. The results of calculations of corresponding energies in cubic and 2H hexagonal structures are compiled in Table 2.

Following a comparison of the total energies of solid solutions in 2H and cubic structures, the 2H structure is energetically preferable for all compositions. Thus, further analysis was carried out for the solid solutions with the hexagonal 2H structure. Based on the total energies of the considered structures, E_{sol}, for $(Ba_{1-x},Sr_x)CoO_3$ and the total energies for parent materials, *e.g.* $BaCoO_3$, and $SrCoO_3$, one can calculate the *mixing energy* of the solid solution, ΔE

$$\Delta E = E_{sol} - ((1 - x)E_{BaCoO_3} + xE_{SrCoO_3}) \quad (2)$$

and perform the analysis of phase stability in terms of the phase diagram (PD) of the corresponding solid solutions.

Calculating ΔE from eqn (2), for all considered compositions, x, we found that $\Delta E > 0$ (Table 2). Thus, the formation of BSC solid solutions is unfavorable at $T = 0$ K, and decomposition of these solid solutions should occur at finite temperatures. Note that at low temperatures this process is expected to be limited by slow diffusion kinetics. ΔE in Table 2 is obtained for several compositions of solid solutions. To construct the PD ΔE should be presented as a function of the atomic fraction of constituents in a whole concentration range, $0 \le x \le 1$. According to the model of regular solid solutions,[44] mixing energy can be expressed in the form

$$\Delta E = Lx(1 - x) \quad (3)$$

where the parameter L is constant and is linked to the mixing potential in solid solution. At the same time, calculations of L for the 2H structure from ΔE given in Table 2 lead to $L = 0.15$ eV, 0.22 eV, and 0.17 eV per formula unit for compositions $x = 0.25$, 0.5, and 0.75, respectively. This demonstrates that L changes as the atomic fraction of Sr is varied. The physical meaning of this effect is clear – it points to the fact that interatomic potentials describing the interaction between Ba atoms, between Sr atoms, and between Ba and Sr atoms on the Ba/Sr sublattice immersed in the field of the rest of the CoO_3 units depend on the atomic fractions of Ba and Sr. This is taken into account in our self-consistent DFT calculations. The obtained result means that the approximation beyond the standard model of regular solid solutions should be applied in the construction of PDs, to describe correctly the mixing on the Ba/Sr sublattice in $Ba_{1-x}Sr_xCoO_3$ solid solutions. Using the Margules polynomial form for the mixing enthalpy[44]

$$H_m^E = (1 - x)x\sum_{i=0}^{n}\lambda_i x^i, \quad (4)$$

keeping in mind that in our case pressure is equal to zero ($H_m^E = \Delta E$) and restricting to $i = 2$, one may express L in the form

$$L = L_0 + L_1x + L_2x^2 \quad (5)$$

with $L_0 = 6 \times 10^{-3}$ eV, $L_1 = 0.2$ eV, $L_2 = -0.19$ eV per site on the Ba/Sr sublattice. These data may be used to construct the quasibinary $BaCoO_3$–$SrCoO_3$ PD. Adding the configuration entropy term the concentration dependence of the *free energy* of formation of solid solution (the free energy of mixing), ΔF may be presented in the following form

$$\Delta F = \Delta E + kT(x\ln(x) + (1 - x)\ln(1 - x)) \quad (6)$$

where ΔE is given by eqn (3) and (5). Eqn (6) is used to construct the PD. In Fig. 2 ΔF is shown for two temperatures, in order to illustrate the way to find the regions of homogeneity of the solid solutions. The common tangent to $\Delta F(x)$ determines the points for binodal (solubility limits) at each temperature. The bending points where the curvature changes from convex to concave

Table 2 Total energies and mixing energy, ΔE, for $Ba_{1-x}Sr_xCoO_3$ solid solutions, in eV per formula unit

x	0	0.125	0.25	0.5	0.75	0.875	1
E_{cub}	−31.79	−31.81	−31.83	−31.88	−31.98	−32.03	−32.08
E_{hex}	−32.84	—	−32.75	−32.66	−32.62	—	−32.59
ΔE_{hex}	0.0		0.028	0.055	0.033		0.0

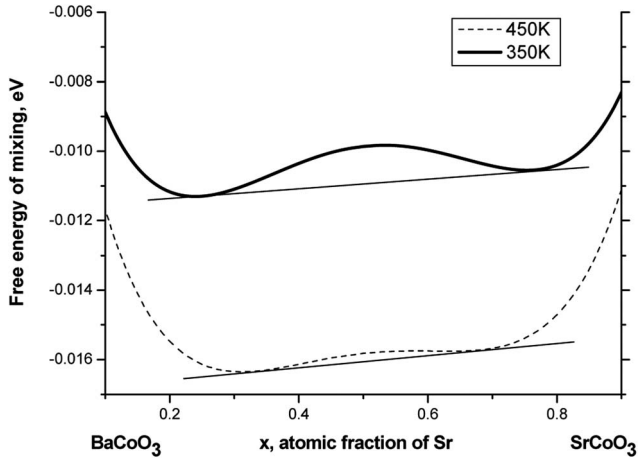

Fig. 2 Free energies of mixing (per atom) for $Ba_{1-x}Sr_xCoO_3$ solid solution corresponding to temperatures 350 K (solid line) and 450 K (dashed line).

(and *vice versa*) give us the atomic fractions that determine the spinodal for each temperature. The calculated PD that illustrates the stability of the quasi-binary solid solution at different temperatures is shown in Fig. 3.

The calculated PD exhibits a miscibility gap, and the decomposition is expected at all temperatures and compositions below the binodal curve. This PD presents the case of the limited solid solubility in the BSCO solid solution. Above relatively low $T = 525$ K the homogeneously disordered $Ba_{1-x}Sr_xCoO_3$ solid solution exists. However, when the temperature decreases below the solubility limit on the PD, the decomposition of the single-phase solid solution into two phases occurs – one enriched in Sr whereas another one depleted in Sr. The fraction of these phases and their compositions are defined by the lever rule applied to the calculated PD. More details about the spinodal decomposition can be found in ref. 21, 44–46.

Note that the decomposition is predicted at relatively low temperatures where thermodynamic measurements may be difficult because of the extremely slow kinetics of cation diffusion in perovskites.[47] It is worth mentioning that the morphologies of the solid solutions in the regions between the binodal and spinodal, and below the spinodal are different. Between the binodal and spinodal the morphology of the two-phase mixture is characterized by well-separated compact clusters of one of the co-existing phases immersed in the matrix of the other phase, while *below* the spinodal the decomposition in two phases leads to the formation of loosely-bound dendrite-like clusters. To be more specific, let us say, when $Ba_{0.65}Sr_{0.35}CoO_3$ homogeneous 2H solid solution is cooled from 500 K to 400 K (*i.e.* to the point between binodal and spinodal, Fig. 3), BSC will decompose into two phases – a relatively small amount of Sr-enriched phase with the composition $Ba_{0.25}Sr_{0.75}CoO_3$ forming separated clusters in the matrix of the Ba-rich $Ba_{0.7}Sr_{0.3}CoO_3$ phase.

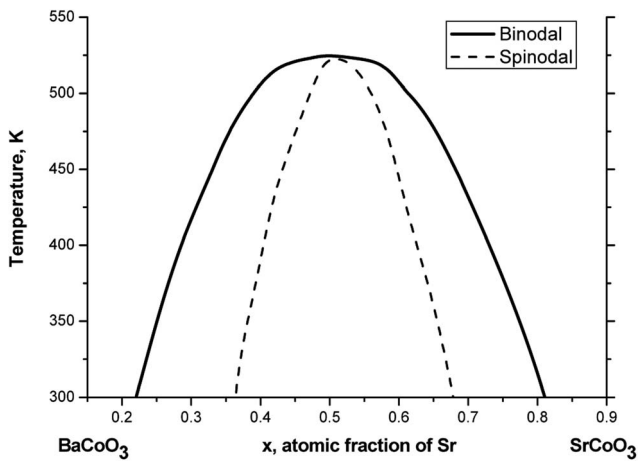

Fig. 3 Quasibinary PD for $Ba_{1-x}Sr_xCoO_3$ solid solution. The solid line is the solubility (binodal) curve and the dashed line shows the region of the spinodal decomposition.

$Ba_{1-x}Sr_xFeO_3$ solid solution

For $Ba_{1-x}Sr_xFeO_3$ (BSF) solid solutions the situation is different. From the results of the total energy calculations for $SrFeO_3$ and $BaFeO_3$ in cubic and 2H structures presented in Table 3, it is seen that the energetically preferable structure for $SrFeO_3$ is cubic, while for $BaFeO_3$ the 2H structure is preferable.

Following a comparison of the total energies of solid solutions in Table 3 in cubic and hexagonal structures, the hexagonal structure is energetically preferable for all compositions $x < 1$. This means that the phase transformation from the hexagonal to cubic structure occurs only when a large amount of Sr is added to $BaFeO_3$, and the decomposition of the solid solution with the co-existing cubic and hexagonal phases should determine the equilibrium state of $Ba_{1-x}Sr_xFeO_3$ at different finite temperatures. To analyze this decomposition, it is necessary to present the mixing energies of the coexisting phases as a function of the atomic fraction of constituents on the Ba/Sr sublattice (as in the previous case) and to study the competition of the phases at different temperatures. In this case the formation of the solid solution should be considered with respect to the mixture of cubic $SrFeO_3$ and 2H $BaFeO_3$. The energies for the cubic and hexagonal structures for different atomic fractions, E_{sol}, are used for the polynomial presentation of the mixing energy

$$\Delta E = E_{sol} - E_{hex}^{BFO}(1 - x) + E_{cub}^{SFO}x = L_0 + L_1x + L_2x^2 + L_3x^3. \quad (7)$$

Note that, on the one hand, such a polynomial form accounts for the deviation from the regular solid solution model (evidently presented by ΔE data in Table 3), and, on the other hand, reflects the differences of the energy for "corner points"

Table 3 Total energies and mixing energy, ΔE, for $Ba_{1-x}Sr_xFeO_3$ solid solutions, in eV per formula unit

x	0	0.125	0.25	0.5	0.75	0.875	1
E_{cub}	−34.66	−34.69	−34.72	−34.76	−34.87	−34.92	−34.97
E_{hex}	−35.19	—	−35.09	−34.99	−34.94	—	−34.90
ΔE_{cub}	0.53	0.47	0.42	0.32	0.16	0.08	0.0
ΔE_{hex}	0.0	—	0.05	0.09	0.08	—	0.07

in quasi-binary solid solution. Indeed, when, let us say, $x = 0$ and E_{sol} is the energy of BFO in the 2H phase, L_0 is equal to zero, while it is equal to the energy difference between cubic and 2H phases of BFO if E_{sol} stands for the energy of the cubic phase. In contrast, if $x = 1$ and E_{sol} is the energy of the cubic phase, then $L_0 + L_1 + L_2 + L_3 = 0$, while if E_{sol} is the energy of the 2H phase the sum $(L_0 + L_1 + L_2 + L_3)$ presents the difference of energies of SFO in cubic and 2H structures.

The parameters L_0, L_1, L_2, and L_3 in eqn (6) differ now for cubic and 2H solid solutions. They may be obtained by fitting of the mixing energy calculated with the data on $\Delta E(x)$ from Table 3 for cubic and hexagonal structures. The accuracy of fitting is illustrated in Fig. 4, whereas parameters are collected in Table 4.

These data were used for constructing the quasibinary PD for $BaFeO_3$–$SrFeO_3$ solid solution. The concentration dependences of the free energies of mixing for both cubic and hexagonal structures are plotted in Fig. 5 at $T = 800$ K. It illustrates the procedure for finding the regions of homogeneity of the solid solutions. Thus, in Fig. 5 $\Delta F^{hex\rightarrow cub}_{BaFeO_3}$ and $\Delta F^{cub\rightarrow hex}_{SrFeO_3}$ show the free energies of BFO transformations (per lattice site) (from 2H to cubic phase) and for SFO (from cubic to 2H phase), respectively. In our case due to inclusion of only configuration entropy and neglect of the phonon contribution to the free energies, these values coincide with corresponding ΔE_{cub} per site for $x = 0$ and ΔE_{hex} per site for $x = 1$ in Table 3, respectively.

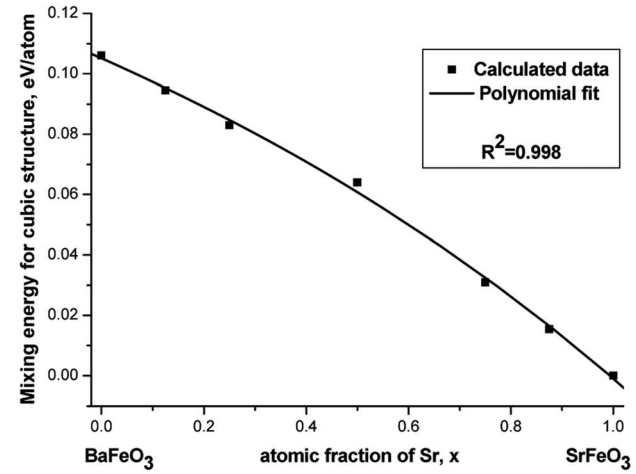

a

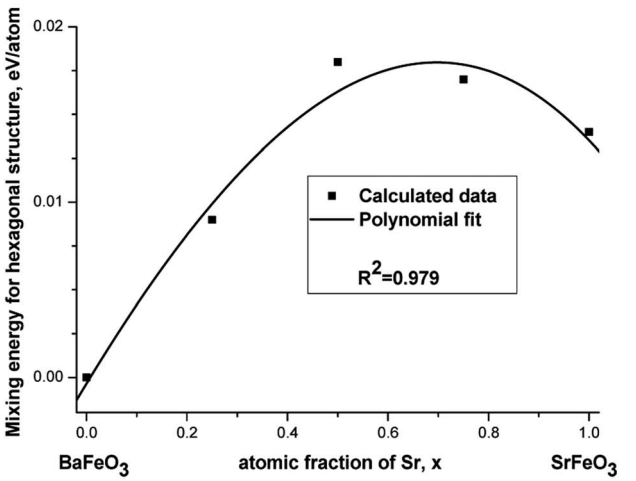

b

Fig. 4 Results of fitting of the mixing energy in cubic (a) and 2H (b) structures for $Ba_{1-x}Sr_xFeO_3$ solid solutions.

Table 4 Interaction parameters that describe the mixing per site on the Ba/Sr sublattice in $Ba_{1-x}Sr_xFeO_3$

Structure/parameters, eV	L_0	L_1	L_2	L_3
Cubic	0.11	−0.08	−0.02	−0.01
Hexagonal	0.0	0.05	−0.02	−0.01

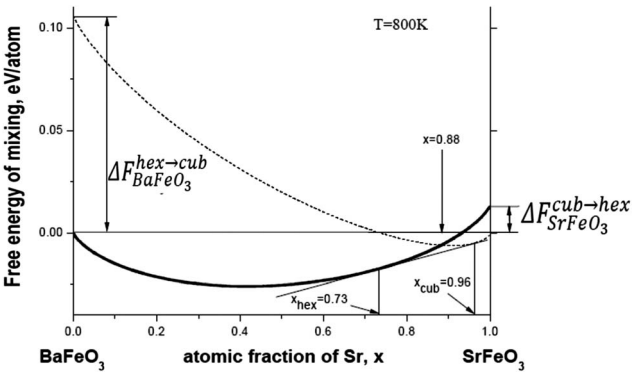

Fig. 5 Schematic illustration of the formation of the heterogeneous mixture of hexagonal and cubic solid solutions at $T = 800$ K. The bold solid line corresponds to the free energy of mixing in the hexagonal structure, while the dashed line corresponds to that in the cubic phase.

The common tangent to *both curves* presenting free energies of mixing in Fig. 5 determines the points for stability limits on PD.

As one can see, although the free energies for 2H and cubic phases are equal at $x = 0.88$, the corresponding state is energetically less favorable compared with the two-phase system described for this composition by the common tangent. This tangent presents the free energy of formation of the heterogeneous mixture of the two phases (2H and cubic), with the compositions $Ba_{0.27}Sr_{0.73}FeO_3$ and $Ba_{0.04}Sr_{0.96}FeO_3$, respectively. In the concentration range $0.73 < x < 0.96$ the free energy presented by this tangent is lower than the free energies of formation of the 2H phase and the cubic phase, and at $T = 800$ K such a two-phase state has to exist. For $x < 0.73$ the homogeneous 2H phase is stable, and as $x > 0.96$, the homogeneous cubic phase exists. Analogous calculations were performed in a wide temperature range, from 400 to 1000 K. Using these data, the quasi-binary PD for $Ba_{1-x}Sr_xFeO_3$ solid solutions was calculated in Fig. 6. (More details on constructing PDs may be found in ref. 48.) The PD demonstrates the decomposition into cubic and hexagonal BSF phases with a pronounced *asymmetric* behavior of the stability limits: a single cubic phase exists only around pure $SrFeO_3$. It is easy to see that if BSF was

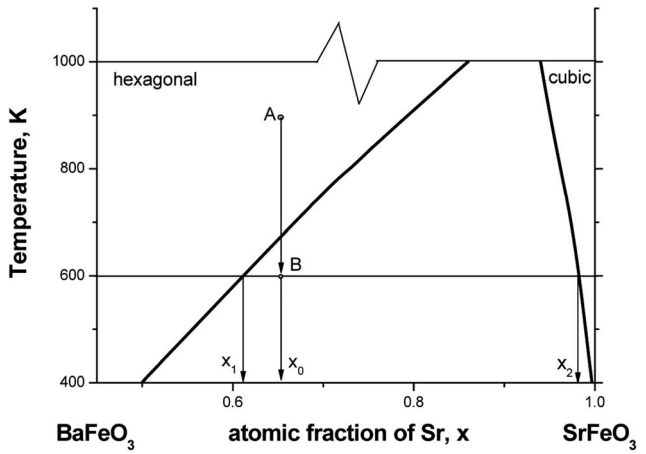

Fig. 6 Quasi-binary PD for $Ba_{1-x}Sr_xFeO_3$ solid solution.

prepared in a single-phase state in the hexagonal structure with the composition $x = x_0$ at temperature ~900 K (point A), after cooling down to $T \sim 600$ K it should decompose into a two-phase mixture. The hexagonal phase in this mixture has the composition $x = x_1$, while in the cubic phase the atomic fraction of Sr is $x = x_2$. As in BSC, the relative fractions of these phases are defined by the lever rule.

Note that we analyze here only the competition of two solid phases, 2H and cubic, and do not take into account the solid and liquid phases; thus the free energy of formation of the liquid state is not considered. Assuming the eutectic type of PD that is quite reasonable in this case (for both BFO and SFO T_{melt} ~ 1500 K (ref. 49 and 50)) and keeping in mind that the eutectic temperature is usually ~20 to 30% smaller than the melting temperature of the edge compounds or elements on PD, we may conclude on the basis of the PD in Fig. 6 that under realistic SOFC conditions ($T = 1100$ K) and the usual composition $x = 0.5$, only the homogeneous hexagonal phase exists. In this phase Ba and Sr atoms statistically occupy the sites of the A-type sub-lattice in BSF.

$SrCo_{1-x}Fe_xO_3$ solid solution

The results of calculations of the SCF solid solution energies in cubic and hexagonal structures are collected in Table 5. The hexagonal structure is energetically preferable in SCF for all compositions $x < 1$, while for $x = 1$ the cubic phase is preferable. Again, it means that the phase transformation from the hexagonal to cubic structure occurs for large x, and the decomposition of the solid solution with the co-existing cubic and hexagonal phases should determine the equilibrium state of SCF at finite temperatures, similar to the case of BCF considered above. We used the equation similar to eqn (7) for the mixing energies for the cubic and hexagonal structures. The parameters L_0, L_1, L_2, and L_3 were obtained again by a fitting of the mixing energy calculated with $E(x)$ in Table 5 for cubic and hexagonal structures. The accuracy of fitting is illustrated in Fig. 7.

The obtained parameters L_0, L_1, L_2, and L_3 are presented in Table 6. These data were used to construct the quasi-binary PD for $SrCoO_3$–$SrFeO_3$ solid solution. The concentration dependence of the free energies of mixing is displayed in Fig. 8,

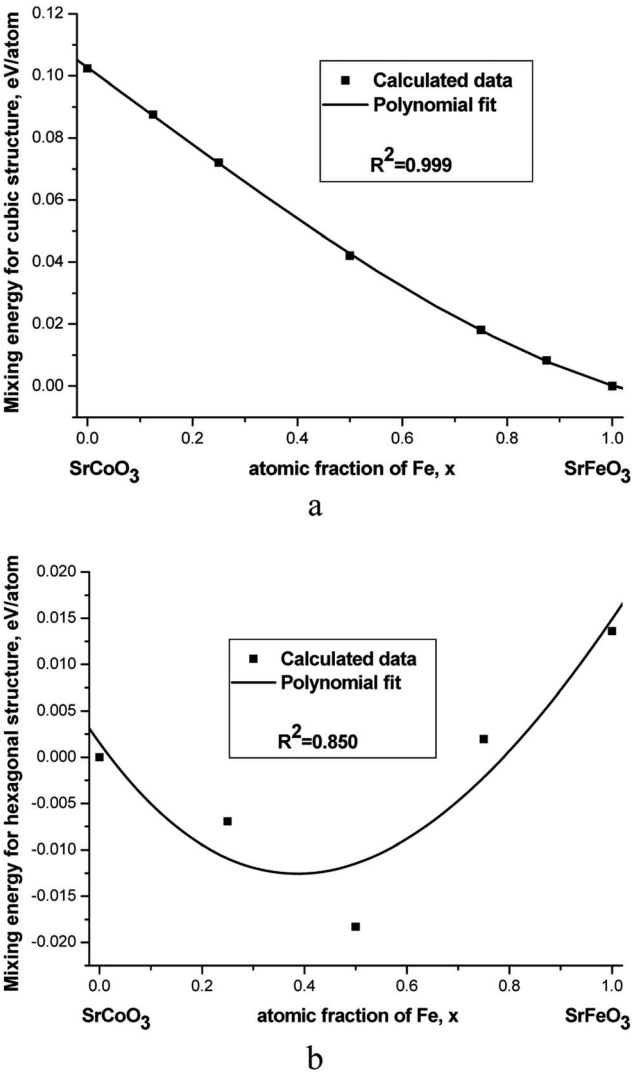

Fig. 7 Results of fitting of the mixing energy in cubic (a) and hexagonal (b) structures for $SrCo_{1-x}Fe_xO_3$ solid solutions.

Table 5 Total energy and mixing energy, ΔE, (in eV) per ABO_3 formula unit for $SrCo_{1-x}Fe_xO_3$ for different atomic fractions, x in cubic and hexagonal (2H) structures

x	0	0.125	0.25	0.5	0.75	0.875	1.0
E_{cub}	−32.077	−32.449	−32.824	−33.569	−34.284	−34.631	−34.970
E_{hex}	−32.589	—	−33.219	−33.871	−34.365	—	−34.902
ΔE_{cub}	0.512	0.438	0.360	0.211	0.091	0.041	0.0
ΔE_{hex}	0.0	—	−0.035	−0.092	0.010	—	0.068

Table 6 Interaction parameters that describe the mixing energy (per lattice site) on the Co/Fe sublattice (in eV)

Structure/parameters	L_0	L_1	L_2	L_3
Cubic	0.103	−0.123	−0.009	0.029
Hexagonal	0.001	−0.076	0.112	−0.024

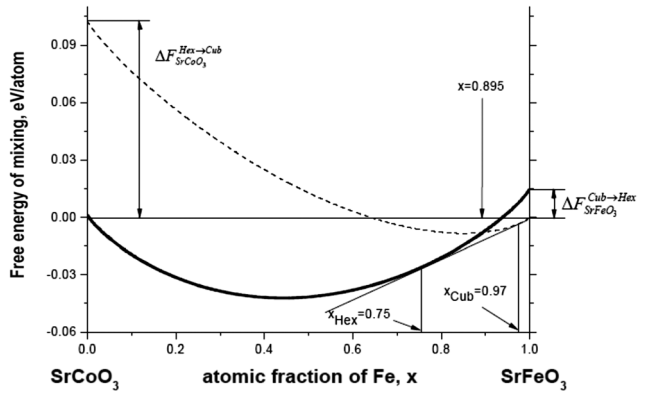

Fig. 8 As shown in Fig. 5 – the heterogeneous mixture of hexagonal and cubic solid solutions at $T = 700$ K. The bold solid line corresponds to the free energy of mixing in the hexagonal structure, while the dashed line corresponds to that in the cubic phase.

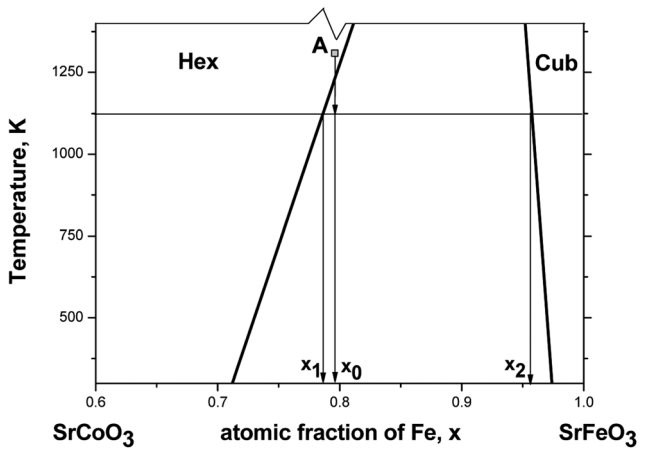

Fig. 9 PD for $SrCo_{1-x}Fe_xO_3$ solid solution.

whereas the PD is shown in Fig. 9. Note that this strongly asymmetric PD is similar to that for BSF. As may be seen from this PD, the homogeneous SCF disordered solid solution at $T \sim$ 1300 K with Co and Fe atoms statistically distributed on the B-sublattice (state A ($x = 0.79$) in Fig. 9) is expected to decompose at $T \sim 1125$ K into the mixture of two phases. At $T \sim 1100$ K for $x \sim 0.5$–0.7 the single-phase $SrCo_{1-x}Fe_xO_3$ solid solution in the hexagonal structure should occur.

Conclusions

Combining the *ab initio* DFT calculations and thermodynamics of solid solutions, we calculated the quasi-binary PDs of several important chemical compositions of BSCF multicomponent perovskites serving as perspective materials for SOFC applications. We predict that the combination of alloying on the A- or B-cation sublattice together with the temperature variation may considerably affect the material properties due to its morphology variations and phase separation. Thus, depending on the type of alloying element and its atomic fraction on the corresponding perovskite sublattice, it is possible to obtain either the homogeneous solid solution or the mixture of two solid solutions with quite different compositions and/or different crystallographic structures. In particular, BSC solid solutions are predicted to show a spinodal decomposition at relatively low temperatures. Although the crystallographic structure of the phases coexisting after the decomposition remains the same in this case, the morphology of the two-phase mixture at low temperatures depends on the state where after cooling the system finds itself – below the spinodal or between the binodal and spinodal.

Note that in BSF and SCF solid solutions the decomposition into two phases is different since both the composition and the crystalline structure of coexisting phases differ as well. The calculated PDs show that the homogeneous one-phase state exists in BSF and SCF around the SOFC operational temperature $T \sim 1100$ K and for solid solution compositions with $x \sim 0.5$. However, decrease of the temperature or varying composition may bring the system into the two-phase state. This effect definitely complicates the design of the complex perovskites with desired properties.

Lastly, it would be of interest to analyze the influence of oxygen vacancies (nonstoichiometry) on the phase stability in the considered solid solutions because real materials usually have some oxygen deficiency. This deviation from the stoichiometry affects the total energies of the considered phases and those of the phases that define the ground state. Remember that the formation energies of the phases are determined as the differences of the total energy for each phase in complex perovskites and the sum of the total energies of the "corner perovskite compounds", weighted with the corresponding atomic fractions of A or B cations on their sub-lattices. Thus, on the one hand, at least for low oxygen deficiency, we do not expect significant nonstoichiometry effects on the considered decomposition trends, mainly due to a substantial compensation of the corresponding energy changes for the calculated cubic and hexagonal phases and for the compounds forming the ground state. On the other hand, to explicitly answer the question, which phases may be formed for high oxygen deficiency, a more complicated approach is necessary. It should be based on the consideration of the *ternary* PD that will include not only a quasi-binary cross-section (Ba/Sr or Co/Fe sublattices as in the cases considered above) but also oxygen at the third corner of the PD. Such a ternary PD demands a huge amount of time-consuming *ab initio* calculations. These calculations have to include the modeling of not only the distribution of Ba/Sr, let us say, on their sublattice but also the modeling of different distributions of oxygen vacancies (in three simple cubic sublattices for cubic phases) for each specific occupation of sites on the Ba/Sr sublattice. Also, there is considerable uncertainty on oxygen deficiency in the materials involved.

Another problem in cases of intermediate and low fraction of oxygen vacancies is the necessity to use extremely large supercells, thus again increasing the computational time. Unfortunately, current computational abilities hardly allow us to perform such types of calculations with the necessary high accuracy and in reasonable time. Even if it were possible, further construction of phase diagrams would be also rather complicated. This would include the modeling of the mixing free energy functions which are the surfaces in the space of atomic fractions of cations and oxygen vacancies. The planes that are tangential to these surfaces will determine the boundaries of the relative stability of competing phases at different temperatures. Thus, the problem on the whole still remains the challenge to the theory.

Note that the importance of the morphology of SOFC materials has already started to attract attention. The attempt to discuss the decomposition in terms of simplistic quarternary PD for the cubic perovskite-type oxide $Ba_xSr_{1-x}Co_{0.8}Fe_{0.2}O_{3-\delta}$ (BSCF) for specific temperatures was reported recently.[51] In order to analyze these experimental data, we performed thermodynamic calculations of the role of oxygen nonstoichiometry in BSCF with a fixed cation composition[25] so that the only variable was oxygen nonstoichiometry.

Acknowledgements

Authors are greatly indebted to R. Merkle and M. M. Kulkja for numerous discussions. This research was partly supported by the GIF research project 1-1025-5-10/2009, Latvian research grant 237/2012, ESF project Nr. 2013/0015/1DP/1.1.1.2.0/13/APIA/VIAA/010 and Juelich Supercomputing Center (project HSS13).

References

1 M. M. Kuklja, E. A. Kotomin, R. Merkle, Yu. A. Mastrikov and J. Maier, *Phys. Chem. Chem. Phys.*, 2013, **15**, 5443.
2 L. Wang, R. Merkle and J. Maier, *J. Electrochem. Soc.*, 2010, **157**, B1802.
3 A. Jacobson, *Chem. Mater.*, 2010, **22**, 660.
4 F. Liang, H. Jiang, H. Luo, J. Caro and A. Feldhoff, *Chem. Mater.*, 2011, **23**, 4765.
5 S. McIntosh, J. F. Vente, W. G. Haije, D. H. A. Blank and H. J. M. Bouwmeester, *Chem. Mater.*, 2006, **18**, 2187.
6 D. Mueller, R. A. De Souza, H.-I. Yoo and M. Martin, *Chem. Mater.*, 2012, **24**, 269.
7 L. Wang, R. Merkle, J. Maier, T. Acartuerk and U. Starke, *Appl. Phys. Lett.*, 2009, **94**, 071908.
8 F. S. Baumann, J. Fleig, H.-U. Habermeier and J. Maier, *Solid State Ionics*, 2006, **177**, 3187.
9 Z. Shao and S. M. Haile, *Nature*, 2004, **431**, 170.
10 S. Svarcova, K. Wiik, J. Tolchard, H. J. M. Bouwmeester and T. Grande, *Solid State Ionics*, 2008, **178**, 1787.
11 R. Kriegel, R. Kircheisen and J. Töpfer, *Solid State Ionics*, 2010, **181**, 64.
12 K. Efimov, Q. Xu and A. Feldhoff, *Chem. Mater.*, 2010, **22**, 5866.
13 S. Yakovlev, C.-Y. Yoo, S. Fang and H. J. M. Bouwmeester, *Appl. Phys. Lett.*, 2010, **96**, 254101.
14 Yu. A. Mastrikov, M. M. Kuklja, E. A. Kotomin and J. Maier, *Energy Environ. Sci.*, 2010, **3**, 1544.
15 E. A. Kotomin, Yu. A. Mastrikov, M. M. Kuklja, R. Merkle, A. Roytburd and J. Maier, *Solid State Ionics*, 2011, **188**, 1.
16 R. Merkle, Yu. A. Mastrikov, E. Kotomin, M. M. Kuklja and J. Maier, *J. Electrochem. Soc.*, 2012, **159**, B212.
17 M. Lumeij, J. Koettgen, M. Gillessen, T. Itoh and R. Dronskowski, *Solid State Ionics*, 2012, **222**, 53.
18 S. Ganopadhyay, A. E. Masunov, T. Inerbaev, J. Mesit, R. K. Guha, A. K. Sleiti and J. S. Kapat, *Solid State Ionics*, 2010, **181**, 1067.
19 M. M. Kuklja, Yu. A. Mastrikov, B. Jansang and E. A. Kotomin, *J. Phys. Chem. C*, 2012, **116**, 18605.
20 R. Merkle, Yu. A. Mastrikov, E. A. Kotomin, M. M. Kuklja and J. Maier, *J. Electrochem. Soc.*, 2012, **159**, B219.
21 D. Fuks, S. Dorfman, S. Piskunov and E. Kotomin, *Phys. Rev. B: Condens. Matter Mater. Phys.*, 2005, **71**, 014111.
22 D. Fuks, L. Bakaleinikov, E. A. Kotomin, J. Felsteiner, A. Gordon, R. A. Evarestov, D. Gryaznov and J. Maier, *Solid State Ionics*, 2006, **177**, 217.
23 A. Weizman, D. Fuks, E. A. Kotomin and D. Gryaznov, *Solid State Ionics*, 2013, **230**, 32; D. Fuks, A. Weizman and E. A. Kotomin, *Phys. Status Solidi B*, 2013, **250**, 864.
24 D. Vingurt and D. Fuks, *Intermetallics*, 2010, **18**, 359.
25 M. M. Kuklja, E. A. Kotomin, D. Fuks, Yu. A. Mastrikov, R. Merkle, O. Sharia and J. Maier, *Chem. Mater.*, 2013, in preparation.
26 G. Kresse and J. Furthmueller, *VASP the Guide*, Univ. Vienna, 2003.
27 H. Ehrenreich and L. M. Schwartz, *Solid State Phys.*, 1976, **31**, 149.
28 J. Cheng, A. Navrotsky, X.-D. Zhou and H. U. Anderson, *Chem. Mater.*, 2005, **17**, 2197.
29 H. Taguchi, Y. Takeda, F. Kanamaru, M. Shimada and M. Koizumi, *Acta Crystallogr., Sect. B: Struct. Crystallogr. Cryst. Chem.*, 1977, **33**, 1299.
30 A. J. Jacobson, *Acta Crystallogr., Sect. B: Struct. Crystallogr. Cryst. Chem.*, 1976, **32**, 1087.
31 H. J. Monkhorst and J. D. Pack, *Phys. Rev. B: Solid State*, 1976, **13**, 5188.
32 P. H. Mayrhofer, D. Music and J. M. Schneider, *Appl. Phys. Lett.*, 2006, **88**, 071922.
33 R. F. Zhang and S. Veprek, *Mater. Sci. Eng., A*, 2007, **448**, 111.
34 I. A. Abrikosov, A. Knutsson, B. Alling, F. Tasnádi, H. Lind, L. Hultman and M. Odén, *Materials*, 2011, **4**, 1599.
35 P. R. Alonso, P. H. Gargano and G. H. Rubiolo, *CALPHAD: Comput. Coupling Phase Diagrams Thermochem.*, 2012, **38**, 117.
36 D. Fuks, S. Dorfman, E. A. Kotomin, Yu. F. Zhukovskii and A. M. Stoneham, *Phys. Rev. Lett.*, 2000, **85**, 433; D. Fuks, E. A. Kotomin, Yu. F. Zhukovskii and A. M. Stoneham, *Phys. Rev. B: Condens. Matter Mater. Phys.*, 2006, **74**, 115418.
37 P. A. Korzhavyi, L. V. Pourovskii, H. W. Hugosson, A. V. Ruban and B. Johansson, *Phys. Rev. Lett.*, 2002, **88**, 015505–015508.

38 A. Bezdicka, J. C. Wattiaux, M. Grenier, P. Pouchard and P. Hagenmuller, *Z. Anorg. Allg. Chem.*, 1993, **619**, 7.
39 Z. Gaoke, L. Ying, Y. Xia, W. Yanping, O. Shixi and L. Hangxing, *Mater. Chem. Phys.*, 2006, **99**, 88.
40 N. Hayashi, T. Yamamoto, H. Kaheyama, M. Nishi, Y. Watanabe, T. Kawakami, Y. Matsushita, A. Fujimori and M. Takano, *Angew. Chem., Int. Ed.*, 2011, **50**, 12547.
41 J. Kirchnerova and D. B. Hibbert, *J. Mater. Sci.*, 1993, **28**, 5800.
42 T. Takeda, Y. Yamaguchi and H. Watanabe, *J. Phys. Soc. Jpn.*, 1972, **33**, 967.
43 C. de la Calle, J. A. Alonso and M. T. Fernandez-Diaz, *Z. Naturforsch. B*, 2008, **63**, 647.
44 Y. Austin Chang and W. Alan Oates, *Materials Thermodynamics*, John Willey&Sons, Inc. Hoboken, New Jersey, 2010, p. 292.
45 K. Binder and P. Fratzl, Spinodal Decomposition, in *Phase Transformation in Materials*, ed. G. Kostorzs, Wiley-VCH, Weinheim, 2001, p. 411.
46 C. N. R. Rao and K. J. Rao, *Phase Transitions in Solids*, McGraw-Hill, New York, 1978, p. 330.
47 S. P. Harvey, R. De Souza and M. Martin, *Energy Environ. Sci.*, 2012, **5**, 5803.
48 L. Kaufman and H. Bernstein, *Computer Calculations of Phase Diagrams*, Academic Press, New York, 1970, p. 334.
49 H. J. Van Hook, *J. Phys. Chem.*, 1964, **68**, 3786.
50 A. Maljuk, J. Strempfer, C. Ulrich, A. Lebon and C. T. Lin, *J. Cryst. Growth*, 2003, **257**, 427.
51 D. N. Mueller, R. A. De Souza, Th. E. Weirich, D. Roehrens, J. Mayer and M. Martin, *Phys. Chem. Chem. Phys.*, 2010, **12**, 10320.

